

Proton-hydrogen collisions at low temperatures

Ming Li* and Bo Gao†

Department of Physics and Astronomy, University of Toledo, Mailstop 111, Toledo, Ohio 43606, USA

(Received 17 October 2014; published 10 March 2015)

We study the proton-hydrogen collision in the energy range from 0 to 5 K where the hyperfine structure of the hydrogen atom becomes important. A proper multichannel treatment of the hyperfine structure is found to be crucial at cold temperatures compared to the elastic approximation traditionally used at higher temperatures. Both elastic and hyperfine-changing inelastic processes are investigated, using both the multichannel quantum-defect theory (MQDT) and the coupled-channel numerical method. Results from the two methods show excellent agreement with MQDT providing an efficient and basically analytic description of the proton-hydrogen interaction throughout this energy range. We also discuss the validity of the elastic approximation and its relation to other methods.

DOI: [10.1103/PhysRevA.91.032702](https://doi.org/10.1103/PhysRevA.91.032702)

PACS number(s): 34.50.Cx, 34.10.+x, 34.70.+e

I. INTRODUCTION

The low-energy proton-hydrogen scattering has been investigated theoretically throughout the past six decades with increasing accuracy and expanding energy range [1–7]. It is important for the understanding of the physics in planetary atmospheres [5,8] and in intergalactic media [9], especially for the interpretation of the brightness of the 21-cm transition, which depends essentially on the spin temperature of atomic hydrogen [8–11].

The proton-hydrogen scattering is also of considerable interest in other contexts. The system itself is one of the arrangements of a fundamental three-body system of $e^- + p + p$. Accurate results for the proton-hydrogen scattering can thus be used as a benchmark for testing three-body theories, in a role similar to the electron-hydrogen scattering in understanding $e^- + e^- + p$ [12,13]. More importantly, an accurate and efficient description of the proton-hydrogen interaction is a prerequisite for understanding other fundamental three-body systems such as $p + H + H$ and $e^- + p + H$, which are of fundamental importance both theoretically and in astronomical applications such as the H_2 formation [14].

While past studies of proton-hydrogen scattering have covered most of the energy range that is of astrophysical interest, the one uncharted territory is the regime of cold and ultracold temperatures. The lowest energy investigated in previous works is 10^{-4} eV [4,6] (equivalent to 1.16 K), which is about an order of magnitude greater than the hyperfine splitting of the atomic hydrogen (equivalent to about 0.07 K), and they have both relied on the elastic approximation [15] that neglects the hyperfine structure. Going below this energy and into the cold and ultracold temperature regimes, the hyperfine interaction is expected to play an important role while the elastic approximation breaks down, similar to what has been shown for the hydrogen-hydrogen scattering using a multichannel numerical method [16].

In this work, we apply the multichannel quantum-defect theory (MQDT) for ion-atom interactions, developed recently [17] that properly accounts for the hyperfine structure, to

provide an efficient and accurate description of the proton-hydrogen scattering in the cold and ultracold regimes. For theoretical understanding and comparison, we also present the results from the coupled-channel (CC) numerical method and discuss the validity of the elastic approximation. The paper is organized as follows. In Sec. II, we outline, in a unified theoretical framework, three methods of treating low-energy proton-hydrogen scattering: the MQDT, the CC numerical method, and the elastic approximation, and discuss their relations. In Sec. III, we compare and discuss the results from different methods, with an emphasis on the cold temperature regime of 0 to 5 K. We conclude in Sec. IV.

II. THEORY

The scattering of a proton with a hydrogen atom in its ground 2S electronic state falls into the category of the atom-ion interaction of the type $^2S + ^1S$ with identical nuclei of spin $I_2 = I_1 = \frac{1}{2}$, which was studied in Ref. [17]. With consideration of the hyperfine structure, all relevant low-energy processes, including elastic, M -changing, and hyperfine-changing processes, can be expressed as

$$H(F_{1i}, M_{1i}) + H^+(F_2, M_{2i}) \longrightarrow H(F_{1j}, M_{1j}) + H^+(F_2, M_{2j}). \quad (1)$$

Here, $F_1 = I_1 \pm \frac{1}{2}$ is the asymptotic total angular momentum corresponding to the 2S electronic state of the hydrogen atom, and $F_2 = I_2 = I_1 = \frac{1}{2}$ is the asymptotic total angular momentum of the proton. The M 's are the corresponding magnetic quantum numbers. The subindices i and j refer to the internal states before and after the collision, respectively.

A. Radial coupled-channel equations

The Hamiltonian describing the system of interest can be written as

$$H = -\frac{\hbar^2}{2\mu} \nabla_R^2 + H_{\text{BO}} + H_{\text{hf}}, \quad (2)$$

where μ is the reduced mass and R is the internuclear distance. H_{hf} represents the hyperfine interaction and H_{BO} is the adiabatic Born-Oppenheimer (BO) Hamiltonian.

*ming.li3@rockets.utoledo.edu

†bo.gao@utoledo.edu

In atomic interactions that involve only S electrons, the total “spin” angular momentum $\mathbf{F} = \mathbf{F}_1 + \mathbf{F}_2$ and the relative orbital angular momentum of the nuclei \mathbf{l} are independently conserved. In this case, the wave function, for each \mathbf{F} and \mathbf{l} , can be written as

$$\psi^{FMlm} = \left[\sum_b \Phi_b^{FM}(\mathbf{R}) G_b^{Fl}(R) / R \right] Y_{lm}(\hat{\mathbf{R}}). \quad (3)$$

Here, M and m are projections of \mathbf{F} and \mathbf{l} on a space-fixed axis, respectively. $\Phi_b^{FM}(\mathbf{R})$ is the channel function of channel b that belongs to an F manifold (the subindex a , used later, also represents a channel that comes from the same set of channels as channel b), $G_b^{Fl}(R)$ is the corresponding radial wave function, and $Y_{lm}(\hat{\mathbf{R}})$ is the spherical harmonics. The angular momentum coupling schemes that define different sets of channel functions are described in the next subsection.

We substitute Eq. (3) into the Schrödinger equation

$$H\psi^{FMlm} = \epsilon\psi^{FMlm}. \quad (4)$$

Upon using the orthogonality properties of the channel functions and ignoring nonadiabatic couplings, we arrive at a set of CC equations for components of G^{Fl} :

$$\left(-\frac{\hbar^2}{2\mu} \frac{d^2}{dR^2} + \frac{l(l+1)\hbar^2}{2\mu R^2} - \epsilon \right) G_a^{Fl}(R) + \sum_b [V_{ab}^{\text{BO}}(R) + V_{ab}^{\text{hf}}(R)] G_b^{Fl}(R) = 0, \quad (5)$$

where

$$V_{ab}^{\text{BO}}(R) \equiv \langle \Phi_a^{FM} | H_{\text{BO}} | \Phi_b^{FM} \rangle, \quad (6a)$$

$$V_{ab}^{\text{hf}}(R) \equiv \langle \Phi_a^{FM} | H_{\text{hf}} | \Phi_b^{FM} \rangle, \quad (6b)$$

both of which are independent of M .

B. Channel structure and frame transformation

For each partial wave l , the total number of states is $2(2I_1 + 1)^2 = 8$, and the total number of channels is $4I_1 + 1 = 3$. These three channels are separated into two uncoupled groups for the two different F 's. For $\frac{1}{2} \leq F \leq 2I_1 - \frac{1}{2}$, which makes $F = \frac{1}{2}$, there are two coupled channels. For $F = 2I_1 + \frac{1}{2} = \frac{3}{2}$, there is only one channel and only elastic scatterings can happen.

We adopt two angular momentum coupling schemes to decompose \mathbf{F} , following the theory of Ref. [18]. The FF coupling scheme $\mathbf{F} = \mathbf{F}_1 + \mathbf{F}_2$ forms the fragmentation channels, or FF channels, that diagonalize the total Hamiltonian when R goes to infinity. The scattering boundary conditions, hence the S matrix, are defined in the FF channels. The JI coupling scheme $\mathbf{F} = \mathbf{J} + \mathbf{I}$ forms the condensation channels, or JI channels, that diagonalize the adiabatic BO Hamiltonian, hence approximately diagonalize the total Hamiltonian in the short range due to the insignificance of the hyperfine interaction in that region. Here, \mathbf{J} is the total electronic angular momentum, which can only have a magnitude of $\frac{1}{2}$, and $\mathbf{I} = \mathbf{I}_1 + \mathbf{I}_2$ is the total nuclear spin. The JI channels are the most directly related to the BO potential curves $^2\Sigma_{g,u}^+$, and are channels in which the short-range K^c matrix of the MQDT

TABLE I. Channel structure for the proton-hydrogen interaction in the ground electronic states. Here, $\mathbf{F} = \mathbf{F}_1 + \mathbf{F}_2$ is the total “spin” angular momentum (including nuclear spin), \mathbf{J} is the total electronic angular momentum, and $\mathbf{I} = \mathbf{I}_1 + \mathbf{I}_2$ is the total nuclear spin.

Total F	FF coupling { F_1, F_2 }	JI coupling { J, I }
$1/2 \leq F \leq 2I_1 - 1/2$	$\{I_1 - 1/2, I_1\}$ $\{I_1 + 1/2, I_1\}$	$\{1/2, F - 1/2\}$ $\{1/2, F + 1/2\}$
$F = 2I_1 + 1/2$	$\{I_1 + 1/2, I_1\}$	$\{1/2, 2I_1\}$

formulation [17] has the simplest representation. The detailed channel structure is illustrated in Table I.

For $F = \frac{1}{2}$, the asymptotic thresholds E_1 and E_2 of the two coupled channels in the FF coupling basis are separated by the atomic hyperfine splitting $E_2 - E_1 = \Delta E^{\text{hf}}$, known as the 21-cm line for hydrogen atoms. It is given by $\Delta E^{\text{hf}}/h \approx 1420.405\,751\,768$ MHz [19] ($\Delta E^{\text{hf}}/k_B \approx 0.068\,168\,729$ K). Following the theory of Ref. [18], the FF and the JI coupling basis functions are related by a frame transformation given by a 2×2 orthogonal matrix

$$U^F = \frac{(-1)^{2F+1}}{\sqrt{2(2I_1+1)}} \times \begin{pmatrix} -\sqrt{2I_1 - F + 1/2} & \sqrt{2I_1 + F + 3/2} \\ \sqrt{2I_1 + F + 3/2} & \sqrt{2I_1 - F + 1/2} \end{pmatrix}. \quad (7)$$

The ordering of the channels here as well as in the matrices later in this paper follows the ordering in Table I.

C. Scattering amplitude and cross sections

The scattering amplitudes for processes of Eq. (1) that satisfy the scattering boundary conditions in the FF channels are given by [18]

$$\begin{aligned} & f(\{F_{1i}M_{1i}, F_{2i}M_{2i}\}\mathbf{k}_i \rightarrow \{F_{1j}M_{1j}, F_{2j}M_{2j}\}\mathbf{k}_j) \\ &= - \sum_{lmFM} \frac{2\pi i}{(k_i k_j)^{1/2}} Y_{lm}^*(\hat{\mathbf{k}}_i) Y_{lm}(\hat{\mathbf{k}}_j) \\ & \quad \times \langle F_{1j}M_{1j}, F_{2j}M_{2j} | F M_F \rangle [S^{Fl}(\epsilon) - \mathbb{1}]_{ji} \\ & \quad \times \langle F M_F | F_{1i}M_{1i}, F_{2i}M_{2i} \rangle, \end{aligned} \quad (8)$$

where $\mathbb{1}$ is the unit matrix and S^{Fl} is the S matrix defined in the FF channels [18]. $\hbar\mathbf{k}_{i,j}$ are the initial and the final relative momenta in the center-of-mass frame.

In terms of the scattering amplitude of Eq. (8), the differential cross section that properly accounts for the symmetry property of identical nuclei is given by [18,20]

$$\begin{aligned} & \frac{d\sigma}{d\Omega_j}(\{F_{1i}M_{1i}, F_{2i}M_{2i}\}\mathbf{k}_i \rightarrow \{F_{1j}M_{1j}, F_{2j}M_{2j}\}\mathbf{k}_j) \\ &= \frac{k_j}{k_i} \frac{1}{2} [|f(i \rightarrow j, \mathbf{k}_j)|^2 + |f(i \rightarrow j, -\mathbf{k}_j)|^2]. \end{aligned} \quad (9)$$

It is symmetric for opposite directions $\hat{\mathbf{k}}_j$ and $-\hat{\mathbf{k}}_j$, as one should expect for identical nuclei.

Many different cross sections can be derived from the differential cross section. In particular, the total cross sections

for elastic (include M -changing) collisions, and the hyperfine excitation and deexcitation processes, after averaging over initial states and summing over final states, are given by

$$\begin{aligned} \sigma(\{F_{1i}, F_2\} \rightarrow \{F_{1j}, F_2\}) \\ = \frac{\pi}{(2F_{1i} + 1)(2F_2 + 1)k_i^2} \sum_{F_l} (2l + 1)(2F + 1) |S_{ji}^{F_l} - \delta_{ji}|^2. \end{aligned} \quad (10)$$

All cross sections are determined by the S matrix, which can be obtained by solving the CC equations using either MQDT or numerical methods, as discussed in the next two subsections.

D. MQDT

One way to obtain the S matrix is MQDT. The MQDT for ion-atom interactions, as demonstrated in Ref. [17], consists of the formulation of Ref. [21] in combination with the QDT functions for the $-1/R^4$ -type potentials as detailed in Ref. [22]. It takes full advantage of the physics that both the energy dependence [23] and the partial wave dependence [24] of the atomic interaction around a threshold are dominated by effects of the long-range potential, which are encapsulated in the universal QDT functions. The short-range contribution is isolated to a short-range K^c matrix that is insensitive to both the energy and the partial wave.

1. General formulation

For an N -channel problem at energies where all channels are open, the MQDT gives the physical K matrix, in our case the K^{Fl} , as [21]

$$K^{Fl} = -(Z_{fc}^c - Z_{gc}^c K^c)(Z_{fs}^c - Z_{gs}^c K^c)^{-1}, \quad (11)$$

where Z_{xy}^c s are $N \times N$ diagonal matrices with elements $Z_{xy}^c(\epsilon_{si}, l)$ being the Z_{xy}^c functions [22] evaluated at the scaled energy $\epsilon_{si} = (\epsilon - \epsilon_i)/s_E$ relative to the respective channel threshold ϵ_i . Here, $s_E = (\hbar^2/2\mu)(1/\beta_4)^2$ and $\beta_4 = (\mu\alpha_A/\hbar^2)^{1/2}$ are the characteristic energy and the length scales, respectively, associated with the polarization potential $-\alpha_A/2R^4$, with α_A being the static polarizability of the atom.

At energies where N_o channels are open, and $N_c = N - N_o$ channels are closed, the MQDT gives [21]

$$K^{Fl} = -(Z_{fc}^c - Z_{gc}^c K_{\text{eff}}^c)(Z_{fs}^c - Z_{gs}^c K_{\text{eff}}^c)^{-1}, \quad (12)$$

where

$$K_{\text{eff}}^c = K_{oo}^c + K_{oc}^c (\chi^c - K_{cc}^c)^{-1} K_{co}^c, \quad (13)$$

in which χ^c is an $N_c \times N_c$ diagonal matrix with elements $\chi_l^c(\epsilon_{si}, l)$ [22], and K_{oo}^c , K_{oc}^c , K_{co}^c , and K_{cc}^c are submatrices of K^c corresponding to open-open, open-closed, closed-open, and closed-closed channels, respectively. Equation (12) is formally the same as Eq. (11), except that the K^c matrix is replaced by the K_{eff}^c that accounts for the effects of the closed channels.

From the physical K matrix, the S matrix is obtained as [18]

$$S^{Fl} = (\mathbb{1} + iK^{Fl})(\mathbb{1} - iK^{Fl})^{-1}. \quad (14)$$

2. K^c matrix and the short-range parametrization

The short-range K^c matrix has only two independent elements, which are two slowly varying functions of energy and l , the single-channel K^c matrices $K_{g,u}^c(\epsilon, l)$ that represent the *gerade* and *ungerade* adiabatic BO molecular states. They are directly related to the corresponding quantum defects $\mu_{g,u}^c(\epsilon, l)$ by [22]

$$K_{g,u}^c(\epsilon, l) = \tan[\pi\mu_{g,u}^c(\epsilon, l) + \pi/4]. \quad (15)$$

For $F = \frac{1}{2}$ where there are two coupled channels, the K^c matrix in the FF channels can be obtained from the one in the Jl channels through the frame transformation, given by

$$K^c = U^{F\dagger} K^{c(Jl)} U^F, \quad (16)$$

where

$$K^{c(Jl)} = \begin{pmatrix} \frac{(K_g^c + K_u^c) + e_2(K_g^c - K_u^c)}{2} & 0 \\ 0 & \frac{(K_g^c + K_u^c) - e_2(K_g^c - K_u^c)}{2} \end{pmatrix}, \quad (17)$$

where $e_2 = (-1)^{F+l-1/2} = (-1)^l$. For $F = \frac{3}{2}$ where there is only one channel, K^c is either given by K_g^c or K_u^c depending on whether $e_1 = (-1)^{2l+1} = (-1)^{l+1}$ is positive or negative:

$$K^c = \frac{1}{2}[(K_g^c + K_u^c) + e_1(K_g^c - K_u^c)]. \quad (18)$$

In the simplest MQDT implementation, instead of two full potential curves used in the numerical calculation, only three constant parameters are needed besides the hyperfine splitting and the reduced mass. The static dipole polarizability of the hydrogen atom $\alpha_A = \frac{9}{2}$ a.u. [25] characterizes the long-range part of the potential. The two QDT parameters, the zero-energy zero angular momentum single-channel $K_{g,u}^c(0, 0)$, characterize the short-range part of the potential due to the energy and partial wave insensitive nature of the short-range interaction. They are related to the corresponding s -wave scattering lengths by [26,27]

$$a_{l=0}^{g,u}/\beta_n = \left[b^{2b} \frac{\Gamma(1-b)}{\Gamma(1+b)} \right] \frac{K_{g,u}^c(0, 0) + \tan(\pi b/2)}{K_{g,u}^c(0, 0) - \tan(\pi b/2)}, \quad (19)$$

where $b = 1/(n-2)$. It reduces to, for $n = 4$ [28],

$$a_{l=0}^{g,u}/\beta_4 = \frac{K_{g,u}^c(0, 0) + 1}{K_{g,u}^c(0, 0) - 1}. \quad (20)$$

More accurate results over a greater range of energies can be obtained by incorporating the energy dependence and, especially, for the range of energy under consideration, the partial wave dependence of the short-range parameters [17]. These weak dependencies are well described by expansions

$$\mu_{g,u}^c(\epsilon, l) \approx \mu_{g,u}^c(0, 0) + b_{g,u}^\mu \epsilon + c_{g,u}^\mu [l(l+1)], \quad (21)$$

in which the parameters $b_{g,u}^\mu$ and $c_{g,u}^\mu$ characterize the energy and the partial wave dependencies of the quantum defects for the *gerade* and *ungerade* states, respectively.

3. Determination of QDT parameters

The simplest MQDT implementation works well for the first handful of partial waves for hydrogen but starts to show noticeable deviation from the numerical calculation when l becomes large, thus it breaks down at energies

TABLE II. Zero-energy QDT parameters used for the comparisons with numerical calculations.

g or u	$K^c(0,0)$	$\mu^c(0,0)$	$a_{l=0}$ (a.u.)	c^μ
<i>Gerade</i>	-0.358 29	0.640 49	-30.371	0.0116
<i>Ungerade</i>	1.1723	0.025 194	810.52	0.0214

where higher partial waves start to contribute significantly. To parametrize the short-range interaction more accurately for energies ranging from ultracold temperatures all the way to 5 K, we need to use the expansion of the quantum defects from Eq. (21).

The zero-energy zero partial wave short-range parameters as well as parameters $b_{g,u}^\mu$ and $c_{g,u}^\mu$ can be determined easily by solving the single-channel radial equations with $V_{g,u}$ as the potential terms at a few energies for a few partial waves. For the energy range considered here, the energy dependence of μ^c is found to be negligible, namely, $b_{g,u}^\mu \approx 0$. To determine the rest of the parameters, we first, for the first several partial waves at zero energy, propagate the radial wave functions through single-channel calculations and match them to the proper scattering boundary conditions, which is given by

$$u_{\epsilon l}(R) = A_{\epsilon l} [f_{\epsilon l}^c(R) - K^c(\epsilon, l) g_{\epsilon l}^c(R)], \quad (22)$$

at progressively larger R until the resulting $K_{g,u}^c$ converge to a desired accuracy [24,26,28,29]. Here, f^c and g^c at $\epsilon = 0$ are the zero-energy QDT reference functions for the $-1/R^4$ potential given in Refs. [27,29]. Then, the resulting $K_{g,u}^c(\epsilon = 0, l)$ are converted into $\mu_{g,u}^c(\epsilon = 0, l)$ and fit into Eq. (21) for various partial waves. The parameters obtained using the potential energy curves constructed in the next section are listed in Table II. The s -wave scattering lengths are calculated using Eq. (20) from the corresponding single-channel K^c 's.

E. Potential energy curves and numerical method

In order to numerically calculate the S matrix to compare to the MQDT results, and also to extract the QDT parameters in this paper, we need to construct the potential energy terms in Eqs. (6a) and (6b) in the FF channels.

For $F = \frac{1}{2}$, there are two coupled channels. The hyperfine term can be approximated as diagonal and constant in the FF channels, which is given by

$$V^{\text{hf}} = \begin{pmatrix} 0 & 0 \\ 0 & \Delta E^{\text{hf}} \end{pmatrix}. \quad (23)$$

The BO potential energy matrix in the FF channels is given in terms of the matrix in the JI channels with a frame transformation, as

$$V^{\text{BO}} = U^{F\dagger} V^{\text{BO}(JI)} U^F. \quad (24)$$

The BO potential energy matrix in the JI channels is diagonal and can be written as

$$V^{\text{BO}(JI)} = \begin{pmatrix} \frac{(V_g + V_u) + e_2(V_g - V_u)}{2} & 0 \\ 0 & \frac{(V_g + V_u) - e_2(V_g - V_u)}{2} \end{pmatrix}, \quad (25)$$

in which $V_{g,u}$ are the two BO potential energy curves for the ${}^2\Sigma_{g,u}^+$ molecular states, respectively.

For $F = \frac{3}{2}$, there is only one channel that only opens when the collision energy is above the upper hyperfine threshold. The hyperfine term $V^{\text{hf}} = \Delta E^{\text{hf}}$, and the BO term is given by

$$V^{\text{BO}} = \frac{1}{2}[(V_g + V_u) + e_1(V_g - V_u)]. \quad (26)$$

To perform the numerical calculation, we need the BO potential energy curves $V_{g,u}$. For the proton-hydrogen interaction, the potential curves can be obtained analytically in the prolate spheroidal coordinates following the method of Ref. [30]. However, to simplify the calculation, we opt for an easier way to construct these potential curves, which is illustrated as follows. For internuclear separation R from 0.4 to 10.0 a.u., we use a cubic spline [31] to interpolate the data points given in Ref. [4] (we will refer to this reference as Paper I) which are calculated using the exact method of Ref. [30]. For R larger than 10.0 a.u., we use the asymptotic expansion from Ref. [25]. More specifically,

$$V_{g,u} = V_0(R) \mp \frac{1}{2} \Delta V(R), \quad (27)$$

with \mp for ${}^2\Sigma_g^+$ and ${}^2\Sigma_u^+$, respectively. Here,

$$V_0(R) = -\frac{9}{4R^4} - \frac{15}{2R^6} - \frac{213}{4R^7} - \frac{7755}{64R^8} - \frac{1773}{2R^9} \quad (28)$$

and

$$\Delta V(R) = 4R e^{-R-1} \left(1 + \frac{1}{2R} - \frac{25}{8R^2} - \frac{131}{48R^3} - \frac{3923}{384R^4} - \frac{145399}{3840R^5} - \frac{521989}{46080R^6} - \frac{509102915}{645120R^7} - \frac{37749539911}{10321920R^8} \right). \quad (29)$$

For R smaller than 0.4 a.u., we use fitted functions for the inner wall, given by

$$V_g(R) = 0.835 \left(\frac{R}{R_0} + 0.0012 \right)^{-1.0597} - 0.993, \quad (30)$$

$$V_u(R) = 0.932 \left(\frac{R}{R_0} - 0.00009 \right)^{-1.031} + 0.0896, \quad (31)$$

in which $R_0 = 1.000544628$ a.u. All the potential equations are in atomic units. The two potential energy curves that we constructed are shown in Fig. 1.

To verify the validity of our potential matrix, we compare the single-channel s -wave short-range parameters in Table II with those from previous works [7,10,32,33]. It was reported that the *ungerade* potential supports two molecular bound states, one of which is extremely weakly bounded with the bound-state energy around 10^{-9} a.u. [33,34]. This extremely weakly bound state makes the evaluation of the corresponding s -wave scattering length very sensitive to the inner potential because the corresponding K^c parameter is very close to 1 [22], which is the singular point in Eq. (20). Thus, it is more straightforward to compare the quantum defects, which behave like phase shifts ranging from 0 to 1, instead of the scattering lengths, because the quantum defects are more evenly defined without any singularity. Comparing the $\mu_{g,u}^c(0,0)$ calculated from the scattering lengths reported in various previous works [7,10,32,33] with our quantum defects, we found the

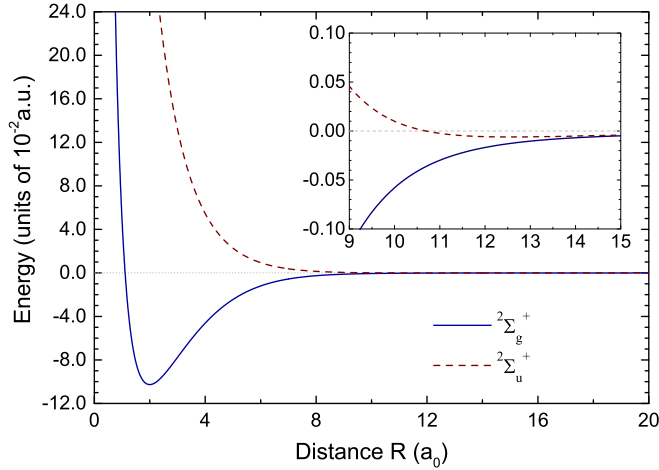


FIG. 1. (Color online) BO potential energy curves of the *gerade* (solid line) and the *ungerade* (dashed line) states constructed in our work for the proton-hydrogen collision.

differences to be only of the order of 10^{-3} , comparing to 1 which is the range of variation of quantum defect. This also confirms the insignificance of the nonadiabatic coupling since the work of Ref. [7] included such coupling term and the work of Ref. [32] used the three-body Faddeev equation. The effect of off-diagonal nonadiabatic coupling can be expected to be similarly small.

In this work, the CC equations are integrated numerically using a hybrid propagator [35,36] constructed similarly to the one used in the HIBRIDON scattering code [37]. It employs a modified version of the log-derivative method of Johnson [38] by Manolopoulos [35] at the short range, and a modified version of the potential-following method of Gordon [39] by Alexander and Manolopoulos [36] at the long range. Convergence can be tested on the resulting S matrix after being converted from the log-derivative matrix following the method of Johnson [38].

F. Elastic approximation

At energies that are much greater than the atomic hyperfine splitting, the hyperfine interaction can be neglected to simplify the theory. Without the hyperfine interaction, the asymptotic states in the Jl channels are degenerate, and the potential matrix is diagonal in the Jl channels in all internuclear separations. Thus, instead of solving the multichannel CC equations in the FF channels, we can solve the single-channel radial equations independently in the Jl channels to obtain the phase shifts for each channel. These phase shifts constitute the physical K matrix in the Jl channels $K^{F(Jl)}$, which can then be transformed to the physical K matrix in the FF channels K^{Fl} , and converted to the S matrix. Such is the essence of the elastic approximation [15], as discussed in Ref. [16].

Under the elastic approximation, for $\frac{1}{2} \leq F \leq 2I_1 - \frac{1}{2}$, the physical K matrix in the Jl channels can be written as

$$K^{F(Jl)} = \begin{pmatrix} \frac{(K_g + K_u) + e_2(K_g - K_u)}{2} & 0 \\ 0 & \frac{(K_g + K_u) - e_2(K_g - K_u)}{2} \end{pmatrix}, \quad (32)$$

where $K_{g,u}(\epsilon, l) = \tan \delta_l^{g,u}(\epsilon)$ with $\delta_l^{g,u}(\epsilon)$ being the single-channel phase shifts of the l th partial wave for the *gerade* state and the *ungerade* state, respectively [28]. These single-channel phase shifts can be calculated from solving the single-channel equations using numerical methods or single-channel QDT [28]. Then, the physical K matrix in the FF channels can be obtained from

$$K^{Fl} = U^{F\dagger} K^{F(Jl)} U^F, \quad (33)$$

and the S matrix can be obtained from Eq. (14). For $F = 2I_1 + \frac{1}{2}$, there is already only a single channel, and no further approximation is necessary.

Applying the elastic approximation using Eqs. (32), (33), and (14), different cross sections can be expressed in terms of $K_{g,u}(\epsilon, l)$ or $\delta_l^{g,u}(\epsilon)$. Here, we present the simplified expressions of the total cross sections given in Eq. (10) under the elastic approximation. For the total cross sections, the zero energy in the elastic approximation, with consideration of the nuclear spin statistics, should be offset from the zero energy in the multichannel treatment by the center of gravity, which is given by $(I_1 + 1)/(2I_1 + 1)\Delta E^{\text{hf}}$.

The hyperfine deexcitation cross section simplifies to

$$\begin{aligned} \sigma_{\text{de}}^{\epsilon \gg \Delta E^{\text{hf}}} & \approx \frac{I_1}{2I_1 + 1} \frac{\pi}{k^2} \sum_{l=0}^{\infty} (2l + 1) \frac{(K_g - K_u)^2}{(1 + K_g^2)(1 + K_u^2)} \\ & = \frac{I_1}{2I_1 + 1} \frac{\pi}{k^2} \sum_{l=0}^{\infty} (2l + 1) \sin^2(\delta_l^u - \delta_l^g), \end{aligned} \quad (34)$$

where σ_{de} is short for $\sigma(\{I_1 + 1/2, I_1\} \rightarrow \{I_1 - 1/2, I_1\})$. This is consistent with the result given in Ref. [40]. If we define the spin-exchange cross section [40] (same as the charge-exchange cross section defined in Ref. [41]) as

$$\sigma_{\text{se}} \equiv \frac{\pi}{k^2} \sum_{l=0}^{\infty} (2l + 1) \sin^2(\delta_l^u - \delta_l^g), \quad (35)$$

Eq. (34) becomes

$$\sigma_{\text{de}}^{\epsilon \gg \Delta E^{\text{hf}}} \approx \frac{I_1}{2I_1 + 1} \sigma_{\text{se}}. \quad (36)$$

The coefficient $I_1/(2I_1 + 1)$ takes into account the nuclear spin statistics, and equals $\frac{1}{4}$ for the proton-hydrogen interaction.

The corresponding hyperfine excitation cross section is related to the deexcitation cross section by a detailed balance relation guaranteed by the time-reversal symmetry [42], which is given by

$$\frac{\sigma_{\text{ex}}}{\sigma_{\text{de}}} = \frac{I_1 + 1}{I_1} \frac{\epsilon - \Delta E^{\text{hf}}}{\epsilon} \stackrel{\epsilon \gg \Delta E^{\text{hf}}}{\approx} \frac{I_1 + 1}{I_1}. \quad (37)$$

σ_{ex} is short for $\sigma(\{I_1 - 1/2, I_1\} \rightarrow \{I_1 + 1/2, I_1\})$, and can be written in terms of the spin-exchange cross section as

$$\sigma_{\text{ex}}^{\epsilon \gg \Delta E^{\text{hf}}} \approx \frac{I_1 + 1}{2I_1 + 1} \sigma_{\text{se}}. \quad (38)$$

Therefore, for the proton-hydrogen system, the coefficient in front of σ_{se} is $\frac{3}{4}$.

For the total elastic cross sections under the elastic approximation, we define the elastic partial wave cross sections

$$\begin{aligned}\sigma_l^{g,u} &\equiv \frac{4\pi}{k^2} (2l+1) \frac{K_{g,u}^2}{1+K_{g,u}^2} \\ &= \frac{4\pi}{k^2} (2l+1) \sin^2 \delta_l^{g,u}\end{aligned}\quad (39)$$

for the *gerade* and the *ungerade* states, respectively. We also define the total elastic cross sections as the summation of the corresponding partial wave cross sections over l , given by

$$\sigma_{\text{tot}}^{g,u} \equiv \sum_{l=0}^{\infty} \sigma_l^{g,u}. \quad (40)$$

The total elastic cross section in the lower hyperfine channel $\sigma_{\text{lo}} \equiv \sigma(\{I_1 - \frac{1}{2}, I_1\} \rightarrow \{I_1 - \frac{1}{2}, I_1\})$ is given by

$$\begin{aligned}\sigma_{\text{lo}} &\stackrel{\epsilon \gg \Delta E^{\text{hf}}}{\sim} \frac{1}{2} (\sigma_{\text{tot}}^g + \sigma_{\text{tot}}^u) + \frac{1}{4I_1 + 2} \sum_{l=0}^{\infty} e_l (\sigma_l^g - \sigma_l^u) \\ &\quad - \frac{I_1 + 1}{2I_1 + 1} \sigma_{\text{se}}.\end{aligned}\quad (41)$$

And, the total elastic cross section in the higher hyperfine channel $\sigma_{\text{hi}} \equiv \sigma(\{I_1 + \frac{1}{2}, I_1\} \rightarrow \{I_1 + \frac{1}{2}, I_1\})$ is given by

$$\begin{aligned}\sigma_{\text{hi}} &\stackrel{\epsilon \gg \Delta E^{\text{hf}}}{\sim} \frac{1}{2} (\sigma_{\text{tot}}^g + \sigma_{\text{tot}}^u) + \frac{1}{4I_1 + 2} \sum_{l=0}^{\infty} e_l (\sigma_l^g - \sigma_l^u) \\ &\quad - \frac{I_1}{2I_1 + 1} \sigma_{\text{se}}.\end{aligned}\quad (42)$$

III. RESULTS AND DISCUSSIONS

A. Multichannel treatment versus elastic approximation

We start with comparing our elastic approximation results of the hyperfine deexcitation cross section with the spin-exchange cross sections given in Paper I, as well as with results from our multichannel treatment. According to Eq. (36), the spin-exchange cross section is four times the hyperfine deexcitation cross section under the elastic approximation for the proton-hydrogen interaction. Therefore, we compare our deexcitation cross-section results with the spin-exchange cross sections given in Paper I multiplied by $\frac{1}{4}$. Also, all the cross-section results from the elastic approximation need to be offset in energy by the center-of-gravity $(I_1 + 1)/(2I_1 + 1) \Delta E^{\text{hf}} = 0.0511265$ K. Our results from both the elastic approximation and the multichannel treatment are obtained using the numerical calculation.

Figure 2 shows the hyperfine deexcitation cross sections, where the data points converted from the results given in Paper I lie right on top of our elastic approximation results. This demonstrates the validity of our potential energy curves and numerical method. The results from the multichannel treatment and the elastic approximation agree almost exactly for energies between 5 and 30 K. The discrepancy between the two becomes more significant when energy decreases especially below 1 K.

Figures 3–5 show the hyperfine excitation cross sections, the elastic cross sections in the lower hyperfine channel, and

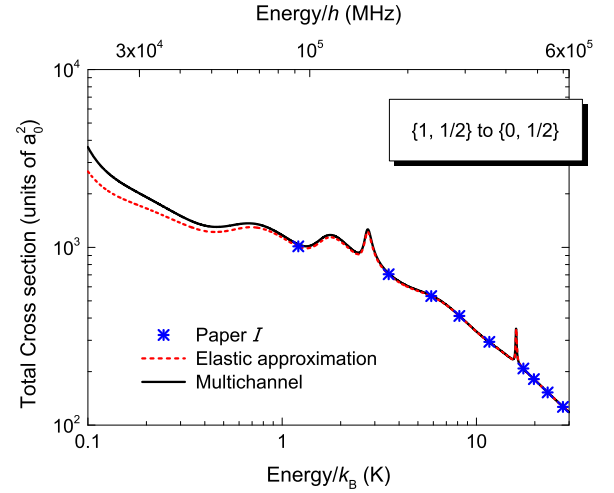


FIG. 2. (Color online) Comparison of the spin-exchange cross section from Paper I multiplied by $\frac{1}{4}$ that accounts for the nuclear statistics (stars) and the total hyperfine deexcitation cross section from channel $\{F_1 = 1, F_2 = \frac{1}{2}\}$ to channel $\{F_1 = 0, F_2 = \frac{1}{2}\}$ using the multichannel treatment (solid line) and the elastic approximation (dashed line).

the elastic cross sections in the higher hyperfine channel, respectively. These comparisons, along with the hyperfine deexcitation case, show that, for the proton-hydrogen interaction, the elastic approximation is applicable for energies larger than 1 K, where it deviates from the multichannel treatment by less than 5%, and becomes more accurate at higher energies, with the deviation becoming less than 1% once the temperature is higher than 5 K. The approximation fails, however, for energies comparable or smaller than the hyperfine splitting. Thus, for temperatures from ultracold up to about 1 K, which is approximately an order of magnitude larger than the hyperfine splitting, the elastic approximation is not

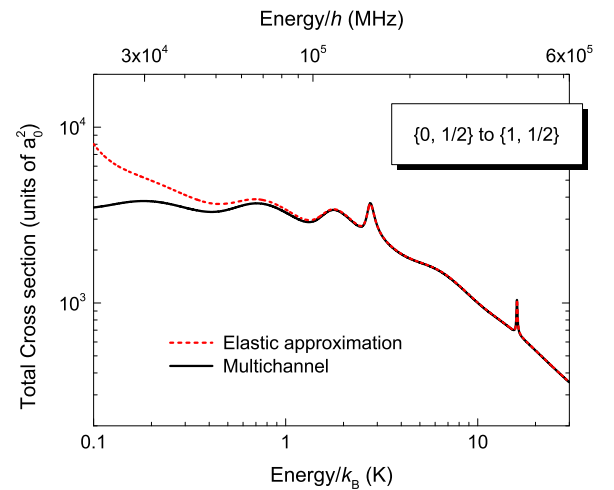


FIG. 3. (Color online) Total hyperfine excitation cross sections from channel $\{F_1 = 0, F_2 = \frac{1}{2}\}$ to channel $\{F_1 = 1, F_2 = \frac{1}{2}\}$ from the elastic approximation (dashed line) and the multichannel treatment (solid line).

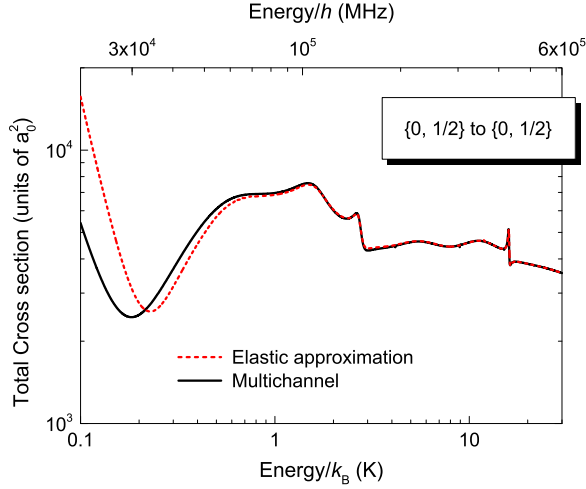


FIG. 4. (Color online) Total elastic cross sections in the lower hyperfine channel $\{F_1 = 0, F_2 = \frac{1}{2}\}$ from the elastic approximation (dashed line) and the multichannel treatment (solid line).

applicable, and multichannel treatment with proper account of the hyperfine interaction should instead be used.

The elastic approximation also gives the incorrect threshold behavior at the upper hyperfine threshold. In previous attempts to extend elastic approximation to lower energy with effective range theory, a constant spin-exchange cross section with the corresponding rate approaching zero was predicted when energy decreases [7,10,11]. With multichannel treatment that incorporates the hyperfine splitting, the deexcitation cross section follows the Wigner's threshold law [43] which diverges as $(\epsilon - E_2)^{-1/2}$ above the upper hyperfine threshold. Therefore, the hyperfine deexcitation rate without thermal averaging

$$\mathcal{W}_{de} \equiv v\sigma_{de} = \sqrt{\frac{2(\epsilon - E_2)}{\mu}} \sigma_{de} \quad (43)$$

will reach a constant when the relative velocity v approaches zero. As illustrated in Fig. 6 with results from multichannel

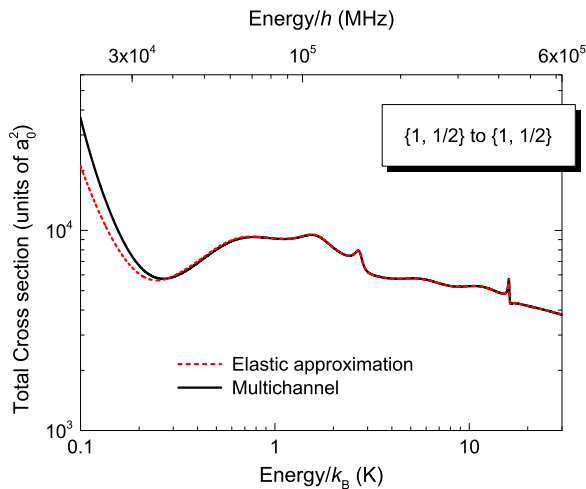


FIG. 5. (Color online) Total elastic cross sections in the upper hyperfine channel $\{F_1 = 1, F_2 = \frac{1}{2}\}$ from the elastic approximation (dashed line) and the multichannel treatment (solid line).

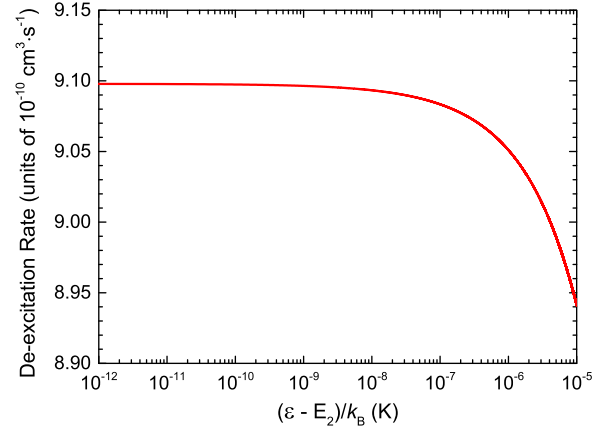


FIG. 6. (Color online) Threshold behavior of the hyperfine deexcitation rate \mathcal{W}_{de} just above the upper threshold E_2 . The x axis represents the temperature equivalence of the initial kinetic energy $(\epsilon - E_2)/k_B$. The results are produced using the multichannel numerical calculation.

numerical calculation, the deexcitation rate rises while initial kinetic energy decreases, until it eventually reaches a plateau with a constant rate of $9.098 \times 10^{-10} \text{ cm}^3 \text{ s}^{-1}$ approximately. The same threshold behavior should also be present for electron-hydrogen and hydrogen-hydrogen collisions.

B. MQDT versus numerical calculation

In this section, we present the total cross section results from ultracold temperature to 5 K using multichannel treatment. In addition, we compare the results from MQDT with the numerical calculation to demonstrate the applicability of MQDT in this temperature regime.

Figure 7 shows the total cross sections for hyperfine deexcitation process from the upper hyperfine threshold to

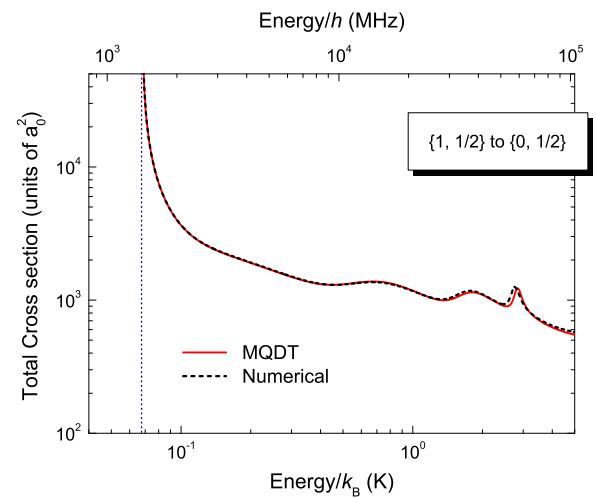


FIG. 7. (Color online) Total hyperfine deexcitation cross sections from channel $\{F_1 = 1, F_2 = \frac{1}{2}\}$ to channel $\{F_1 = 0, F_2 = \frac{1}{2}\}$ from MQDT (solid line) and numerical method (dashed line). The vertical dashed line identifies the upper hyperfine threshold located at $\epsilon_2/k_B \approx 0.0682 \text{ K}$, around which the cross section diverges as $(\epsilon - E_2)^{-1/2}$.

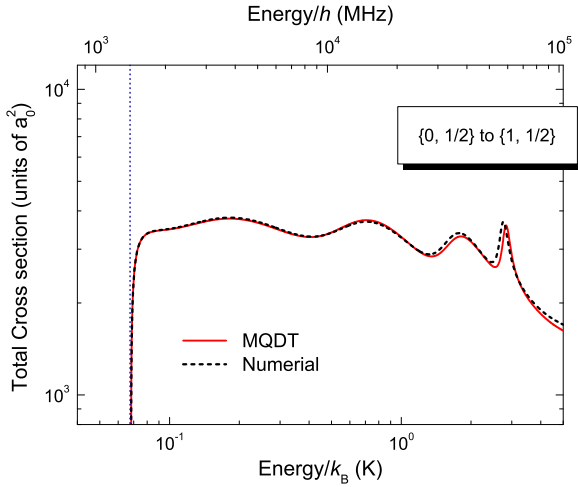


FIG. 8. (Color online) Total hyperfine excitation cross sections from channel $\{F_1 = 0, F_2 = \frac{1}{2}\}$ to channel $\{F_1 = 1, F_2 = \frac{1}{2}\}$ from MQDT (solid line) and numerical method (dashed line). The vertical dashed line identifies the upper hyperfine threshold located at $\epsilon_2/k_B \approx 0.0682$ K, around which the cross section behaves as $(\epsilon - E_2)^{1/2}$.

5 K. Notice that, as mentioned in the previous section, the deexcitation cross section follows the Wigner's threshold law [43], which diverges as $(\epsilon - E_2)^{-1/2}$ above the upper hyperfine threshold. MQDT results are almost exactly on top of the numerical calculation below 1 K, and, although there is slight deviation, the two methods still agree relatively well from 1–5 K. The discrepancy is in general within 1% which can be attributed to slight energy dependence of the short-range QDT parameters.

Figure 8 shows the total cross sections for hyperfine excitation in which the hydrogen atom is excited from its $F_1 = 0$ hyperfine state to its $F_1 = 1$ hyperfine state. It behaves as $(\epsilon - E_2)^{1/2}$ above the upper threshold. The excitation cross section is related to the deexcitation cross section by Eq. (37) which is guaranteed by the time-reversal symmetry [42].

Figures 9 and 10 depict the total cross sections for elastic scattering in the lower hyperfine channel and the higher hyperfine channel, respectively, in which the atom remains in the same hyperfine level after the scattering while its M_1 may or may not change. The elastic cross section in the higher hyperfine channel, just like the deexcitation cross section, diverges as $(E - E_2)^{-1/2}$ above the upper threshold, implying a constant rate in the zero-temperature limit.

Compared to our previous results on the resonant charge-exchange problem of $^{23}\text{Na} + ^{23}\text{Na}^+$ [17], there are not any significant resonance structures within the hyperfine splitting for the proton-hydrogen system, even though the hyperfine splittings of the two systems are of the same order of magnitude. This can be attributed to the small atomic mass and polarizability of hydrogen which give an unusually large energy scale $s_E = 0.0416$ K for the proton-hydrogen system compared to other ion-atom systems (e.g., $s_E = 2.21 \mu\text{K}$ for $^{23}\text{Na} + ^{23}\text{Na}^+$). With such a large energy scale, the hyperfine splitting corresponding to a scaled energy of $\Delta E^{\text{hf}}/s_E \approx 1.6$ is much smaller in magnitude than the energy bin of $B_{-1}(l=0) = -105.81$ that contains the least bound s state [22,44],

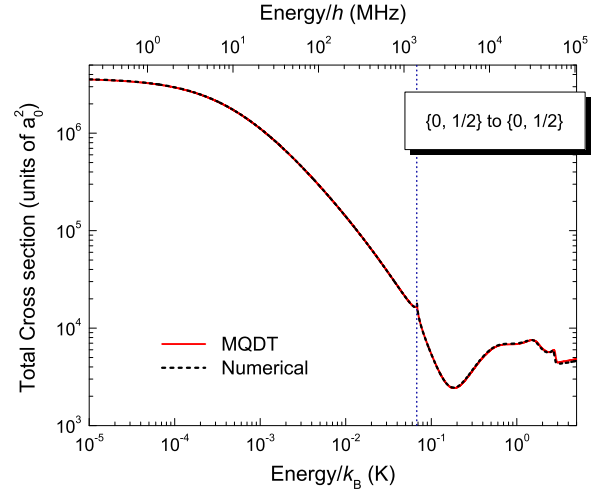


FIG. 9. (Color online) Total elastic cross sections in the lower channel $\{F_1 = 0, F_2 = \frac{1}{2}\}$ from MQDT (solid line) and numerical method (dashed line). The vertical dashed line identifies the upper hyperfine threshold at 0.0682 K.

and even smaller compared to energy bins that contain the least bound states of higher partial waves. There is thus little probability that a Feshbach resonance associated with the upper threshold can appear within the hyperfine interval. Similarly, the probability for the appearance of a shape resonance associated with the lower threshold is very small. As for the diffraction resonances [17,22,44], the scaled energy of the hyperfine splitting is too small to support any. The only resonances in proton-hydrogen scattering are the shape and diffraction resonances above the upper hyperfine threshold. There are two relatively visible features in all four figures. The broader feature around 1.7 K corresponds to a shape resonance in partial wave $l = 3$, and the sharper feature around 2.8 K corresponds to a shape resonance in partial wave $l = 4$. There

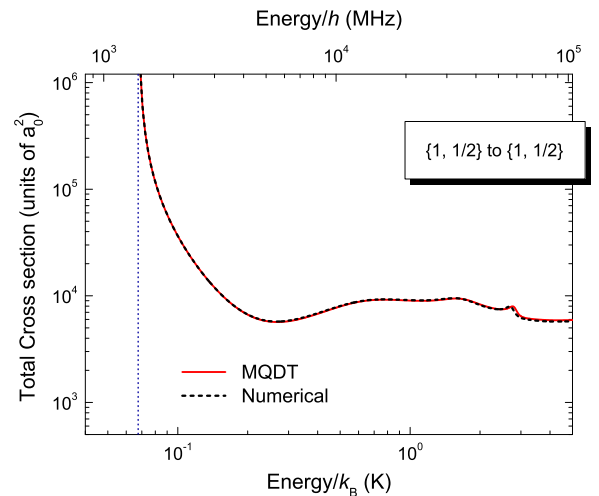


FIG. 10. (Color online) Total elastic cross sections in the upper channel $\{F_1 = 1, F_2 = \frac{1}{2}\}$ from MQDT (solid line) and numerical method (dashed line). The vertical dashed line identifies the upper hyperfine threshold at 0.0682 K.

is another sharp feature around 16 K, shown in Figs. 2 through 5 from the previous subsection, which corresponds to a shape resonance in partial wave $l = 7$.

Figures 8–10 are similar to Fig. 7 in showing the agreement between results from MQDT and the numerical calculation, and the conclusion we drew for the deexcitation cross section case also stands for the others. The deviation of the MQDT results from the numerical results is within 2% for temperatures lower than 1 K, and is within 5% for temperatures from 1 to 5 K, for both the background and the resonance positions. This again demonstrates the capability of MQDT to accurately characterize multichannel ion-atom interactions from zero energy up to several kelvin with only a handful of parameters (five in this case), as we have demonstrated before on the example of sodium resonant charge exchange [17]. Also examined and verified by these comparisons is the physical picture behind the MQDT formulation, that in this energy regime, the energy and partial wave dependencies are primarily due to the long-range interaction which can be accurately characterized by the analytic solution of the long-range potentials, and the short-range parameters are energy and partial wave insensitive [21,22].

Computationally, MQDT is much more efficient than the numerical calculation even when the QDT functions are calculated on the fly. Since the QDT functions are universal mathematical functions that are the same for all applications and can be computed to arbitrary precision with efficient algorithms [22], their computation can be further accelerated to be as efficient as most other mathematical special functions.

This computational advantage will be even more pronounced in other applications with more coupled channels.

IV. CONCLUSIONS

In summary, we have investigated the low-energy proton-hydrogen interaction using three different methods: the CC numerical method, the MQDT, and the elastic approximation. The results show that at energies comparable or smaller than the hyperfine splitting, the effect of nuclear spin is no longer merely statistical, but has to be treated in a multichannel framework using either the CC numerical method or MQDT. The differences between single and multichannel treatments are not only quantitative, but qualitative in nature for the threshold behavior. The MQDT method provides a simple, systematic, and quantitatively accurate description of proton-hydrogen interaction in this difficult multichannel regime. Its simplicity and efficiency suggest the potential and the promise of MQDT and its off-shell generalization in future studies of three-body processes such as those involving $p + H + H$ or $e^- + p + H$.

ACKNOWLEDGMENTS

We thank L. You and M. K. Tey for helpful discussions. This work was supported in part by NSF (US National Science Foundation) under Grant No. PHY-1306407. B.G. also acknowledges partial support by NSFC (National Natural Science Foundation of China) under Grant No. 11328404.

-
- [1] A. Dalgarno and H. N. Yadav, *Proc. Phys. Soc. London, Sect. A* **66**, 173 (1953).
 - [2] D. R. Bates and A. H. Boyd, *Proc. Phys. Soc. London* **80**, 1301 (1962).
 - [3] F. J. Smith, *Planet. Space Sci.* **14**, 929 (1966).
 - [4] G. Hunter and M. Kuriyan, *Proc. R. Soc. London, Ser. A* **353**, 575 (1977).
 - [5] R. R. Hodges and E. L. Breig, *J. Geophys. Res.* **96**, 7697 (1991).
 - [6] P. S. Krstić, J. H. Macek, S. Y. Ovchinnikov, and D. R. Schultz, *Phys. Rev. A* **70**, 042711 (2004).
 - [7] E. Bodo, P. Zhang, and A. Dalgarno, *New J. Phys.* **10**, 033024 (2008).
 - [8] D. L. Huestis, *Planet. Space Sci.* **56**, 1733 (2008).
 - [9] A. A. Meiksin, *Rev. Mod. Phys.* **81**, 1405 (2009).
 - [10] A. E. Glassgold, P. S. Krstić, and D. R. Schultz, *Astrophys. J.* **621**, 808 (2005).
 - [11] S. R. Furlanetto and M. R. Furlanetto, *Mon. Not. R. Astron. Soc.* **379**, 130 (2007).
 - [12] H. Bürger, W. Sandhas, and E. O. Alt, *Phys. Rev. A* **30**, 2965 (1984).
 - [13] C.-R. Liu, B. Gao, and A. F. Starace, *Phys. Rev. A* **46**, 5985 (1992).
 - [14] W. D. Watson, *Rev. Mod. Phys.* **48**, 513 (1976).
 - [15] A. Dalgarno, *Proc. R. Soc. London, Ser. A* **262**, 132 (1961).
 - [16] B. Zygelman, A. Dalgarno, M. J. Jamieson, and P. C. Stancil, *Phys. Rev. A* **67**, 042715 (2003).
 - [17] M. Li, L. You, and B. Gao, *Phys. Rev. A* **89**, 052704 (2014).
 - [18] B. Gao, *Phys. Rev. A* **54**, 2022 (1996).
 - [19] H. Hellwig, R. F. C. Vessot, M. W. Levine, P. W. Zitzewitz, D. Allan, and D. Glaze, *IEEE Trans. Instrum. Meas.* **19**, 200 (1970).
 - [20] B. Gao, *Phys. Rev. A* **87**, 059903(E) (2013).
 - [21] B. Gao, E. Tiesinga, C. J. Williams, and P. S. Julienne, *Phys. Rev. A* **72**, 042719 (2005).
 - [22] B. Gao, *Phys. Rev. A* **88**, 022701 (2013).
 - [23] B. Gao, *Phys. Rev. A* **58**, 4222 (1998).
 - [24] B. Gao, *Phys. Rev. A* **64**, 010701(R) (2001).
 - [25] R. J. Damburg and R. K. Propin, *J. Phys. B: At. Mol. Phys.* **1**, 681 (1968).
 - [26] B. Gao, *J. Phys. B: At., Mol. Opt. Phys.* **36**, 2111 (2003).
 - [27] B. Gao, *Euro. Phys. J. D* **31**, 283 (2004).
 - [28] M. Li and B. Gao, *Phys. Rev. A* **86**, 012707 (2012).
 - [29] B. Gao, *Phys. Rev. A* **78**, 012702 (2008).
 - [30] G. Hunter, B. F. Gray, and H. O. Pritchard, *J. Chem. Phys.* **45**, 3806 (1966).
 - [31] W. H. Press, S. A. Teukolsky, W. T. Vetterling, and B. P. Flannery, *Numerical Recipes: The Art of Scientific Computing*, 3rd ed. (Cambridge University Press, Cambridge, 2007).
 - [32] J. Carbonell, R. Lazauskas, D. Delande, L. Hilico, and S. Kl, *Europhys. Lett.* **64**, 316 (2003).
 - [33] A. Kaiser, T.-O. Müller, and H. Friedrich, *Mol. Phys.* **111**, 878 (2013).
 - [34] J. Carbonell, R. Lazauskas, and V. I. Korobov, *J. Phys. B: At., Mol. Opt. Phys.* **37**, 2997 (2004).

- [35] D. E. Manolopoulos, *J. Chem. Phys.* **85**, 6425 (1986).
- [36] M. H. Alexander and D. E. Manolopoulos, *J. Chem. Phys.* **86**, 2044 (1987).
- [37] HIBRIDON[®] is a package of programs for the time-independent quantum treatment of inelastic collisions and photodissociation written by M. H. Alexander, D. E. Manolopoulos, H.-J. Werner, and B. Follmeg, with contributions by P. F. Vohralik, D. Lemoine, G. Corey, R. Gordon, B. Johnson, T. Orlikowski, A. Berning, A. Degli-Esposti, C. Rist, P. Dagdigian, B. Pouilly, G. van der Sanden, M. Yang, F. de Weerd, S. Gregurick, and J. Klos.
- [38] B. R. Johnson, *J. Comput. Phys.* **13**, 445 (1973).
- [39] R. G. Gordon, *J. Chem. Phys.* **51**, 14 (1969).
- [40] A. Dalgarno and M. R. H. Rudge, *Proc. R. Soc. London A* **286**, 519 (1965).
- [41] R. Côté and A. Dalgarno, *Phys. Rev. A* **62**, 012709 (2000).
- [42] L. D. Landau and E. M. Lifshitz, *Quantum Mechanics* (Pergamon, Oxford, 1977).
- [43] E. P. Wigner, *Phys. Rev.* **73**, 1002 (1948).
- [44] B. Gao, *Phys. Rev. Lett.* **104**, 213201 (2010).